



Article

Ultrabroadband Absorption Enhancement via Hybridization of Localized and Propagating Surface Plasmons

Tian Sang ^{1,*} , Honglong Qi ¹, Xun Wang ¹, Xin Yin ¹, Guoqing Li ¹, Xinshang Niu ², Bin Ma ² and Hongfei Jiao ^{2,*}

¹ Department of Photoelectric Information Science and Engineering, School of Science, Jiangnan University, Wuxi 214122, China; 18860478830@163.com (H.Q.); wangxun1012gg@163.com (X.W.); xinyin0202@163.com (X.Y.); 18351037802@163.com (G.L.)

² Key Laboratory of Advanced Micro-Structured Materials MOE Institute of Precision Optical Engineering, School of Physics Science and Engineering, Tongji University, Shanghai 200092, China; 1631921@tongji.edu.cn (X.N.); mabin@tongji.edu.cn (B.M.)

* Correspondence: sangt@jiangnan.edu.cn (T.S.); jiaohf@tongji.edu.cn (H.J.)

Received: 27 July 2020; Accepted: 16 August 2020; Published: 19 August 2020



Abstract: Broadband metamaterial absorbers (MAs) are critical for applications of photonic and optoelectronic devices. Despite long-standing efforts on broadband MAs, it has been challenging to achieve ultrabroadband absorption with high absorptivity and omnidirectional characteristics within a comparatively simple and low-cost architecture. Here we design, fabricate, and characterize a novel compact Cr-based MA to achieve ultrabroadband absorption in the visible to near-infrared wavelength region. The Cr-based MA consists of Cr nanorods and Cr substrate sandwiched by three pairs of SiO₂/Cr stacks. Both simulated and experimental results show that an average absorption over 93.7% can be achieved in the range of 400–1000 nm. Specifically, the ultrabroadband features result from the co-excitations of localized surface plasmon (LSP) and propagating surface plasmon (PSP) and their synergistic absorption effects, where absorption in the shorter and longer wavelengths are mainly contributed by the LSP and PSP modes, respectively. The Cr-based MA is very robust to variations of the geometrical parameters, and angle- and polarization-insensitive absorption can be operated well over a large range of angles under both transverse magnetic (TM)- and transverse electric (TE)-polarized light illumination.

Keywords: metamaterial absorbers; ultrabroadband absorption; localized surface plasmon; propagating surface plasmon

1. Introduction

Light absorption enhancements in metamaterials have received intensive attention due to their diverse performances in a series of applications such as thermal emitters [1,2], sensors [3–5], photodetectors [6,7], photovoltaics [8,9], and optical imaging devices [10–12]. In general, the typical design scheme for a metamaterial absorber (MA) consists of sandwiched metal-insulator-metal (MIM) layers with the patterned top surface [13]. In these structures, the electric dipole resonance can be induced by the metallic patterns and the magnetic dipole resonance can be excited by the anti-parallel currents between the interfaces of the metal and insulator layers. By using different patterned surfaces such as strip [14], square [15], hole [16], and disk [17], perfect absorption can be achieved as the impedance of the structure equals that of the incident medium at a specific frequency. Furthermore, by using more sophisticated metallic patterns such as crossed trapezoid [18], nanostars [19], and square ring [20], the absorption bandwidth can be improved to cover the whole visible region. However,

the absorption bandwidth of the MIM-based MA is relatively narrow due to the resonance effect of the magnetic or electric dipole.

To extend the bandwidth, multi-sized resonators with patterns such as strips [21,22], patches [23,24], ellipses [25], and crosses [26] can be integrated together to form a supercell, and the absorption bandwidth of the multi-sized MA can be effectively improved due to the blending of multiple resonant frequencies. Unfortunately, the achievable bandwidth is limited because the number of possible integrated resonators in a supercell is restricted. Moreover, with the increase of the number of the resonators, the effective number density of each resonator decreases, resulting in deterioration of the overall absorption performances [27].

In recent years, hyperbolic metamaterials (HMMs) have been deemed a valuable class of optical metamaterials to enhance light-matter interaction due to the anisotropic optical response. Such anisotropic behavior is accompanied by an isofrequency surface in the shape of a hyperboloid, which supports propagating high wavevector modes and demonstrates an enhanced photonic density of states [28–30]. Moreover, HMMs have been demonstrated to enable a tailored control of light extinction, scattering, and absorption processes [31–33], to achieve resonant gain singularities [34] and enhanced spontaneous emission rates of molecules [35–37]. Recently, a mechanism has been proposed to achieve high absorption (experimentally >90%, theoretically approaching 99%) in the near-infrared region [38], where hybrid localized propagating modes are responsible for the excitation of highly absorptive Bloch Plasmon polariton modes supported by the multilayered HMM structure. Similarly, near-perfect absorption is also achievable by exploiting the direct excitation of localized and/or propagating modes within the HMM structures [39–41]. In particular, the taped metal/dielectric stack-based HMMs, such as sawtooths [42–44], nano-cones [45–47], and pyramids [48,49], showing the hyperbolic dispersion diagram, enable broadband light absorption enhancement due to the collective excitation of slow-light waveguide modes, i.e., the trapped rainbow effect [50,51]. Although the absorption performances of the taped metal/dielectric stack-based HMMs are striking, their fabrication procedure is quite challenging because graded width of metal/dielectric patterns as well as a large number of thin-film stacks are required. Noble metals are used widely in most MAs due to their excellent performance supporting surface plasmon polaritons at optical frequencies, which leads to expensive cost in the fabrication process. From the point of view of application, despite the elaborate study of MAs, further performance improvements in absorption efficiency, bandwidth, and most importantly omnidirectional features are highly desired.

Herein, we propose a novel architecture of Cr-based MA with subwavelength thickness to achieve ultrabroadband, angle- and polarization-insensitive absorption in the visible and near-infrared regions. The Cr-based MA consists of Cr nanorods and Cr substrate sandwiched by three pairs of SiO₂/Cr stacks. Both simulated and experimental results indicate that an average absorption over 93.7% can be achieved at wavelengths ranging from 400 to 1000 nm. The physical basis for the ultrabroadband absorption is the hybridization of localized and propagating surface plasmon modes, where absorption enhancement in the shorter and longer wavelengths are mainly contributed from the localized surface plasmon (LSP) and propagating surface plasmon (PSP) modes, respectively. Moreover, the absorption performances of the Cr-based MA are insensitive to variations of the structural parameters, and the broadband features can be maintained even at the incident angle of 60° for both transverse magnetic (TM) and transverse electric (TE) polarizations. All these advantageous optical properties make our proposed structure a good candidate to improve various important applications such as photovoltaic devices, remote sensing and photodetectors.

2. Design and Characterization of the Proposed MA

Figure 1a shows the schematic diagram of the proposed MA and its absorption response under normal illumination of the transverse magnetic (TM) or transverse electric (TE) plane wave. The inset is the side view of the Cr-based MA, and the structural parameters of the unit cell are labeled in the figure caption. The Cr-based MA consists of Cr nanorods and Cr substrate sandwiched by three pairs

of SiO₂/Cr stacks, and the Cr nanorods and SiO₂/Cr stacks are separated by a SiO₂ buffer layer with the thickness h_1 . The period of the unit cell is P , the height and diameter of the Cr nanorods are h and d , respectively; t_m and t_d are the thickness of Cr and SiO₂ of the film stacks, respectively. The refractive index of SiO₂ is 1.47, and the complex refractive indices of the Cr film are obtained from Rakic et al. [52].

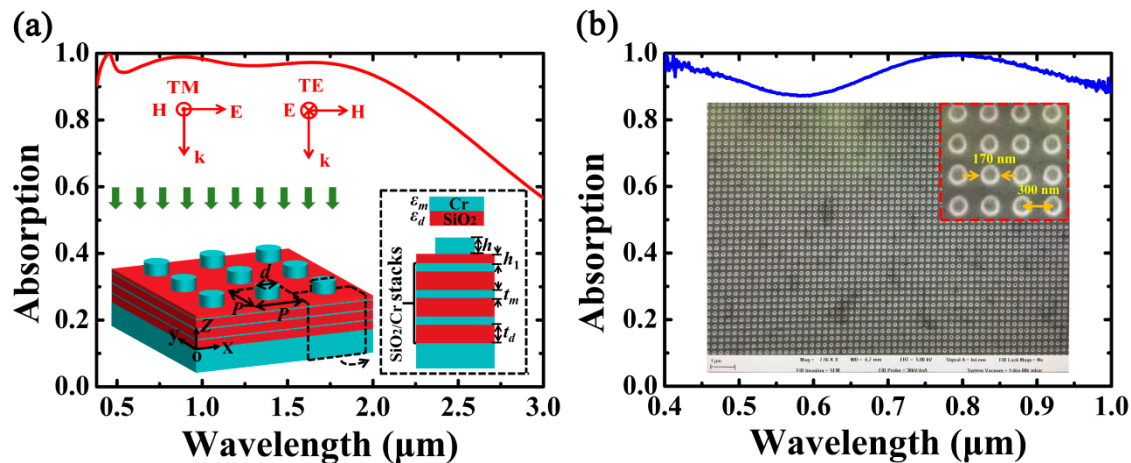


Figure 1. (a) A schematic diagram of the Cr-based metamaterial absorber (MA) and its simulated absorption in the designed wavelength region. The parameters are: $P = 300$ nm, $d = 165$ nm, $h = 100$ nm, $h_1 = 28$ nm, $t_m = 6$ nm, and $t_d = 85$ nm. (b) The measured absorption and the SEM image of the fabricated MA with a zoomed SEM image in the inset.

In simulations, a finite-difference time-domain (FDTD) approach is adopted to calculate the absorption of the Cr-based MA using the commercial software Lumerical [53]. At normal incidence, periodic boundary conditions are used in the x and y directions with Bloch/periodic plane wave type, and a perfectly matched layer is used in the z direction. However, Bloch boundary conditions need to be chosen in the x and y directions with BFAST plane wave type at oblique incidence. The grid sizes in the x , y and z directions are 1.5 nm \times 1.5 nm \times 1.5 nm, respectively. The absorption of the total structure can be reduced as $A(\lambda) = 1 - R(\lambda)$ because there is no transmission for the optically thick Cr substrate, where $R(\lambda)$ is the reflection of the structure. In addition, the absorption of different parts of the Cr-based structure can be calculated by integrating power dissipation in the desired part of the unit cell [15,54]:

$$P_{\text{abs}} = \frac{1}{2} \epsilon_0 \omega \text{Im}(\epsilon) \int_V |E|^2 dV \quad (1)$$

where ϵ_0 is the vacuum permittivity, ω is the angular frequency, ϵ is the relative dielectric permittivity, and $\text{Im}(\epsilon)$ is its imaginary part; $|E|$ denotes the electric-field amplitude.

In addition, to compare the absorption bandwidth of the proposed MA with other types of MAs, we define the relative absorption bandwidth (RAB) as:

$$\text{RAB} = 2(\lambda_L - \lambda_S) / (\lambda_L + \lambda_S) \quad (2)$$

where λ_L and λ_S are the larger and smaller limits of wavelength with the absorptivity greater than 90%, and the average absorption within the operating wavelength region can be calculated as $A_{\text{av}} = \frac{1}{\lambda_L - \lambda_S} \int_{\lambda_S}^{\lambda_L} A(\lambda) d\lambda$.

In Figure 1a, the absorption response of the Cr-based MA is calculated as $A = (A_{\text{TM}} + A_{\text{TE}})/2$, where A_{TM} and A_{TE} are the absorption of the TM and TE polarizations, respectively. As shown in Figure 1a, ultrabroadband absorption can be realized at wavelengths ranging from 380.0 to 2137.5 nm with absorptivity higher than 90% and average absorption of $A_{\text{av}} = 96.4\%$. The RAB of the Cr-based MA is 139.6%, which is larger than many types of MAs such as MIM-based MAs [13–20], multi-sized MAs [21–26], and HMM-based MAs [42–46]. In addition, although only three metal/dielectric stacks are required,

the RAB of the Cr-based MA is also comparable with those of the MAs such as multilayered-based nanocones [47] and pyramids [48,49]. Therefore, the proposed MA possesses the advantages of combining excellent absorption performance with comparatively simple and low-cost configuration.

The SEM image of the fabricated MA and the experimental absorption spectrum are depicted in Figure 1b. The Cr-based MA is achieved by combining the thin-films deposition with nanorod array fabrication. In the process of Cr/SiO₂ thin-films deposition, we used the e-beam evaporation coater (OTFC-1300, OPTORUN Co. Ltd., Saitama, Japan) which was equipped with two JEOL electron guns and an ion-source. The Cr substrate, SiO₂/Cr stacks, and SiO₂ buffer layer were deposited alternatively by OTFC-1300 on K9 glasses with a diameter of 25 mm. The Cr films were deposited by e-beam evaporation with a deposition rate of 0.7 nm/s and pressure of 4.3×10^{-3} Pa; the SiO₂ films were deposited by ion-assisted deposition with a deposition rate of 0.8 nm/s and pressure of 7.3×10^{-3} Pa. The Cr nanorod arrays were fabricated as follows. Firstly, a 380 nm thick e-beam resist (Zep 520) was spin-coated with 4000 rpm on the Cr/SiO₂ thin-films and baked on a hotplate at 180 °C for 180 s. Then, the resist layer with an area of $180 \times 180 \mu\text{m}$ was exposed by e-beam writing (JEOL 6300 FS; JEOL Ltd., Akishima, Japan) at 100 kV with a 7 nm beam size. After e-beam exposure, the development process was carried out to realize nanohole arrays using amyl acetate for 70 s, and then isopropyl alcohol (IPA) rinse for 60 s. Finally, a 100 nm thick Cr film was deposited on the nanohole array via e-beam evaporation, and the remained e-beam resist was removed by N-Methyl-2-Pyrrolidinone (NMP) and DI water to obtain the proposed MA.

In Figure 1b, the reflection spectra of the sample are measured by an angle-resolved microspectroscope (AR-ARM; Ideaoptics Instruments Co. Ltd., China). A 100 W halogen lamp is used to produce a broadband illumination. Measurement is set to an area about $80 \times 80 \mu\text{m}$ using a $100 \times$ microscope objective lens with a numerical aperture of 0.9. Reflection spectra $R(\lambda)$ were normalized to a silver mirror with 96% reflectivity in the designed wavelength region, and the measured absorption of the sample can be obtained as $A(\lambda) = 1 - R(\lambda)$. Herein, the wavelength range is confined within 400–1000 nm due to the limitation of detectability of the silicon-based photodetector of our measured system. As can be seen in Figure 1b, the measured results agree well with the simulations in structural profile as well as absorption performance, and an average absorption of 93.7% can be achieved within the wavelength region of 400–1000 nm. However, there are some mismatches between the simulation and experimental results; for example, the two absorption peaks in the shorter and longer wavelengths in simulation are 451.2 nm and 884.5 nm, respectively; while in experiment they are blue-shifted to 418.8 nm and 802.8 nm, respectively. The discrepancies may result from fabrication errors, such as surface/edge roughness of the Cr nanorods, and deviations in the realized dimensions. In addition, the inconsistent permittivity of Cr between the simulation and experiment is also responsible for the mismatches between the simulation and experimental results.

3. Physical Basis for Ultrabroadband Absorption Enhancement

To better understand the physical basis for ultrabroadband absorption of the proposed MA, the absorption of the total structure and its distributions in different parts of the structure are shown in Figure 2a. As can be seen in Figure 2a, the absorption of the total structure is mainly contributed by the SiO₂/Cr stacks, and the absorption of the Cr substrate is comparably low in the whole wavelength region. However, absorption contributed by the Cr nanorods plays an important role in realizing high-efficiency absorption of the total structure; in particular, a large amount of absorption is resulted from the Cr nanorods in the short wavelength region. To corroborate the correlation between the absorption performances and the related electromagnetic parameters of the Cr-based metasurface, here we investigate the input impedances of the total structure by using the impedance theory. Based on

the impedance theory [55,56], the impedance Z of the Cr-based MA can be obtained by the extraction of the scattering parameters as follows:

$$Z = \pm \sqrt{\frac{(1 + S_{11})^2 - S_{21}^2}{(1 - S_{11})^2 - S_{21}^2}} \quad (3)$$

$$S_{11} = S_{22} = \frac{i(1 - Z^2) \sin(nkD)}{2Z} \quad (4)$$

$$S_{21} = S_{12} = \frac{4}{4 \cos(nkD) - i(2Z + 1) \sin(nkD)} \quad (5)$$

where S_{11} , S_{22} , S_{21} , S_{12} are S parameters; k , n , and D are the wave vector, the effective refractive index, and thickness of the structure, respectively. The reflection of the Cr-based MA can be calculated as $R = [(Z - Z_0)/(Z + Z_0)]^2$, where Z and Z_0 are the normalized impedance of the structure and free space, respectively. In simulation, S parameters of the Cr-based metasurface are complex amplitude reflection and transmission coefficients, which can be obtained by using the S parameters analysis group of Lumerical. As can be seen in Figure 2b, the real part of Z tends to 1 and its imaginary part approaches 0 in the range of 0.38–2.14 μm , leading to the ultrabroadband antireflection effect with $R \approx 0$ in the wavelength region of interest.

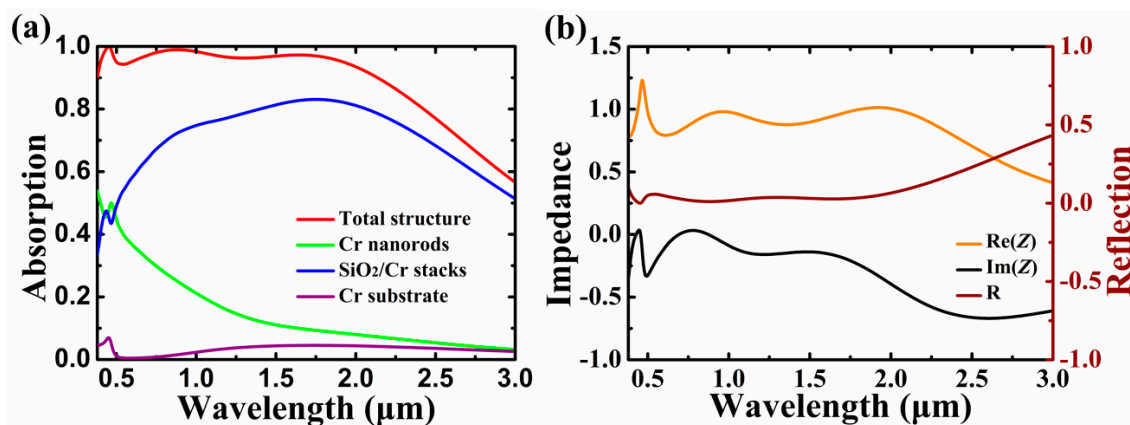


Figure 2. (a) Absorption of the Cr-based MA and its absorption distributions in different parts of the structure. (b) Impedance and reflection curves of the Cr-based MA. Other parameters are kept the same as Figure 1a.

To gain further insight into the ultrabroadband absorption enhancement of the Cr-based MA, distributions of electromagnetic field, Poynting vector, and current density associated with the absorption peaks are shown in Figure 3. As can be seen in Figure 3a–c, the normalized amplitudes of the electric field of the absorption peaks are distinctly enhanced, and four hotspots occur at both the top and bottom edges of the Cr nanorods, indicating the excitation of LSP, which has a dipolar feature [57,58]. Moreover, the Poynting vector distribution shows that the energy of the incident light primarily flows and dissipates around the Cr nanorods, and more light will penetrate into the SiO₂/Cr stacks as resonance wavelength is increased. In Figure 3d, the normalized magnetic field distribution shows that the excitation of PSP is evident in the region among the neighboring Cr nanorods, while a large amount of PSP simultaneously propagates into the SiO₂/Cr stacks and Cr substrate via the buffer layer as well. Note that the magnetic field distribution in Figure 3d is more localized in the SiO₂/Cr stacks by comparison with that shown in Figure 3e,f due to its high quality resonance feature. In Figure 3e,f, it can be seen that the ratio of PSP that propagates into the SiO₂/Cr stacks is increased for the longer wavelength, which exhibits a similar trend to that of the Poynting vector distributions in Figure 3b,c. Therefore, the co-excitations of LSP and PSP and their synergistic absorption effects

strongly improve the interaction between light and Cr material, resulting in ultrabroadband absorption of the Cr-based MA with subwavelength thickness. Figure 3g–i shows that the current densities of the absorption peaks are simultaneously enhanced in the Cr nanorods, Cr stacks, and Cr substrate, and the ratio of the current density in the Cr stacks is increased for the longer wavelength, indicating that the absorption contributed by the SiO₂/Cr stacks will be increased with the increase of absorption wavelength, a result which is in line with the results in Figure 2a.

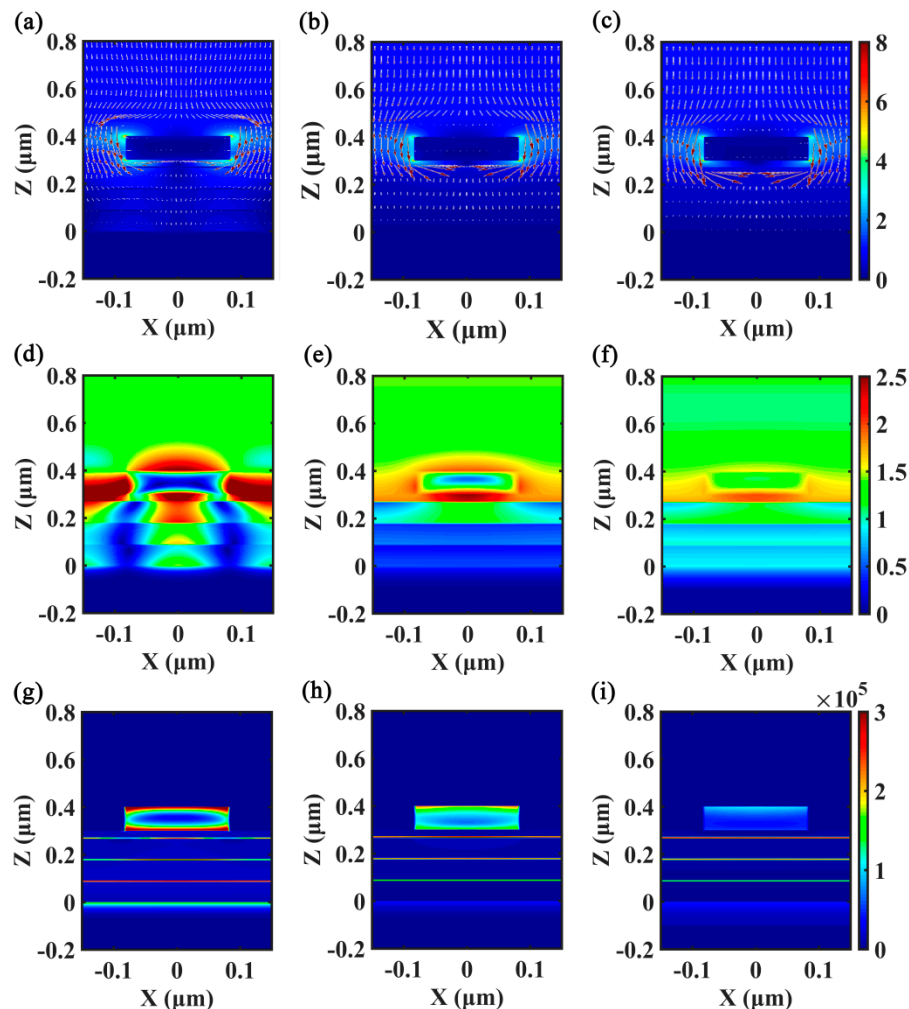


Figure 3. Distributions of electromagnetic field, Poynting vector, and current density associated with the absorption peaks of the Cr-based MA. Other parameters are the same as Figure 1a. (a–c) are the near field distributions of $|E|$ and Poynting vector at 451.2 nm, 884.5 nm, and 1642.3 nm, respectively. The red arrow indicates the direction of Poynting vector. (d–f) are the near field distributions of $|H|$ at 451.2 nm, 884.5 nm, and 1642.3 nm, respectively. (g–i) are the distributions of current density at 451.2 nm, 884.5 nm, and 1642.3 nm, respectively.

4. Evaluation of Absorption Performances of the Proposed MA

To evaluate the robustness of absorption performances of the proposed MA, we first investigate the influences of the geometrical parameters (d , h , h_1 , P , t_d , t_m) on the absorption responses of the Cr-based MA. As can be seen in Figure 4a, the Cr-based MA shows broadband absorption features as d varied in the range of 75–195 nm, and good absorption performances that combine the merits of both broadband absorption and high absorption efficiency can be realized around $d = 165$ nm. Figure 4b shows that ultrabroadband absorption can be realized as the height of the Cr nanorods is large enough ($h > 70$ nm), while the absorption performances will be degraded if h is too small, due to the coupling of the surface plasmons between the top and bottom surfaces of the Cr nanorod. In Figure 4c, it can

be seen that the absorption performance of the Cr-based MA is not good without the buffer layer ($h_1 = 0$); however, the absorption curves deteriorate and the absorption band splits as $h_1 > 50$ nm. By properly selecting the thickness of the buffer layer such as $h_1 = 28$ nm, the absorption bandwidth can be effectively improved due to electromagnetic coupling between the Cr nanorods and SiO₂/Cr stacks. As Figure 4d shows, broadband absorption enhancement can be maintained even if period is significantly varied. However, in the deep-subwavelength region ($P < 200$ nm), the absorption is reduced significantly due to the increase in reflection of the structure. In Figure 4e, it can be seen that the absorption bandwidth can be enlarged by increasing t_d ; however, the absorption performances possessing ultrabroadband and high absorption efficiency will be best near $t_d = 85$ nm. In Figure 4f, it can be seen that the absorption bandwidth can be significantly improved around $t_m = 5$ nm. Note that broadband absorption will be reduced to two absorption bands as $t_m = 0$; the absorption band near $\lambda = 0.39$ μm is associated with the LSP, while the absorption band near $\lambda = 0.80$ μm arises from the excitation of gap plasmon of the MIM-based structures [59,60].

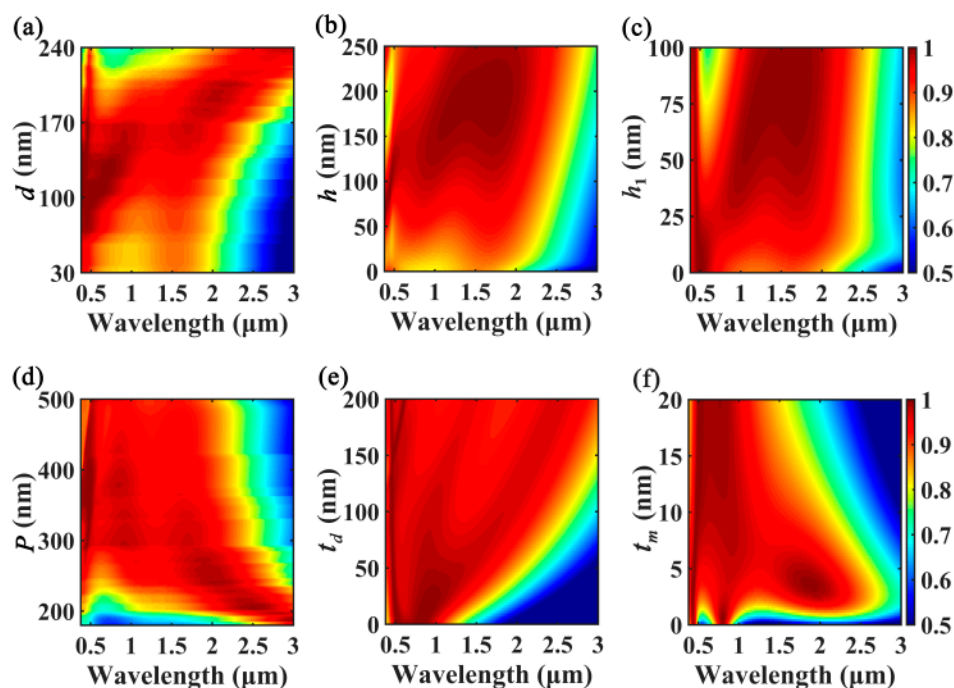


Figure 4. Absorption 2D map of the Cr-based MA as functions of (a) diameter of the Cr nanorods d , (b) height of the Cr nanorods h , (c) thickness of the buffer layer h_1 , (d) period P , (e) thickness of SiO₂ film t_d , and (f) thickness of Cr film t_m . Other parameters are kept the same as Figure 1a.

We further characterized the incident angle dependence of the Cr-based MA under the illumination for both the TM and TE polarizations. As shown in Figure 5a, the absorption spectra exhibit omnidirectional features in the designed wavelength region in the case of TM polarization. The absorbing properties can be kept almost the same even the incident angle θ is significantly altered, and an average absorption of 90.8% can be obtained in the wavelength range of 380.0–2137.5 nm as $\theta = 60^\circ$. In Figure 5b, it can be seen that the Cr-based MA shows good absorption performances in experiment within the range of 400–1000 nm. In Figure 4c, it can be seen that the absorption performances of the Cr-based MA can be maintained well for TE polarization within $\pm 60^\circ$; however, the intensity of the absorption and the absorption bandwidth drops quickly when the incident angle is larger than 60° . In the case of TE wave illumination, the tangential component of magnetic incident field decreases as $\theta > 60^\circ$, the magnetic coupling and the incident magnetic flux between the metallic films is reduced, thus less light energy could be absorbed effectively due to the impedance mismatch [61–63]. As can be seen in Figure 5d, the measured curves show broadband absorption features, although they vary more obviously as θ increases, in comparison with those of the TM polarization.

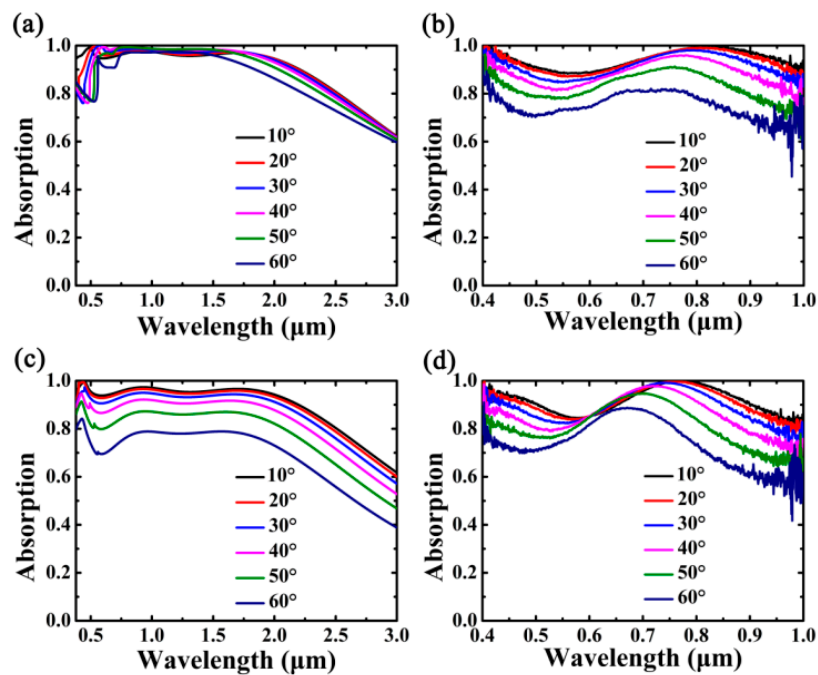


Figure 5. Absorption curves of the Cr-based MA at oblique incidence. Other parameters are kept the same as Figure 1a. (a,b) are the simulated and measured absorption of TM polarization, respectively. (c,d) are the simulated and measured absorption of TE polarization, respectively.

The influences of polarization angle on absorption performances of the Cr-based MA are shown in Figure 6. As can be seen in Figure 6a, absorption of the Cr-based MA is immune to the variation of the polarization angle due to the symmetrical topology. As the polarization angle is altered from 0° to 90° , that is, from TM polarization to TE polarization, ultrabroadband absorption performance of the Cr-based MA remains the same. In Figure 6b, it can be seen that the measured absorption spectra are insensitive to the variation of the polarization angle. Therefore, the proposed Cr-based MA is angle- and polarization-insensitive and can be operated well for both the TM and TE polarizations.

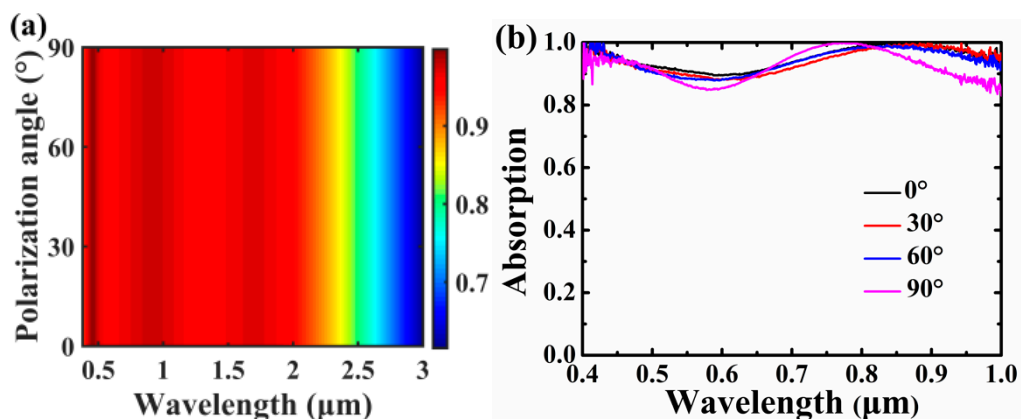


Figure 6. Absorption spectra of the Cr-based MA under the variation of polarization angle. Other parameters are kept the same as Figure 1a. (a) Theoretical absorption 2D map as a function of polarization angle. (b) Measured absorption spectra as a function of polarization angle.

5. Summary

In conclusion, we have designed, fabricated, and characterized an ultrabroadband Cr-based MA in the visible to near-infrared region. Ultrabroadband absorption with $RAB = 139.6\%$ and average absorption of 96.4% can be realized within the range of $380.0\text{--}2137.5\text{ nm}$ in design, and an average

absorption of 93.7% can be achieved in the 400–1000 nm wavelength range in experiment. The absorption enhancement results from the co-excitations of LSP and PSP and their synergistic absorption effects, which ensure the ultrabroadband features via the Cr-based MA with subwavelength thickness. The Cr-based MA is very robust to variations of the geometrical parameters, and ultrabroadband performances can be maintained even if the structural parameters are significantly altered. In addition, our device exhibits omnidirectional features in the designed region within $\pm 60^\circ$ for the TM polarization, and angle- and polarization-insensitive absorption can be operated well under both TM and TE-polarized light illumination. The proposed scheme combines the advantages of both LSP and PSP modes in a low-cost and comparatively simple architecture, which will be beneficial for various interesting applications such as photodetection, energy harvesting, and thermal emitters.

Author Contributions: T.S. and H.Q. performed simulations and optical measurements, fabricated the nanorod arrays, and drafted the manuscript; X.W., X.Y., and G.L. checked the data and improved visualization. X.N., B.M., and H.J. fabricated the thin-films and checked the manuscript. All authors have read and agreed to the published version of the manuscript.

Funding: This research was funded by National Natural Science Foundation of China (Grant Nos. 61975155, 61975153), and Major Projects of Science and Technology Commission of Shanghai (Grant No. 17JC1400800).

Conflicts of Interest: The authors declare no conflict of interest.

References

1. Liu, X.; Tyler, T.; Starr, T.; Starr, A.F.; Jokerst, N.M.; Padilla, W.J. Taming the blackbody with metamaterials as selective thermal emitters. *Phys. Rev. Lett.* **2011**, *107*, 045901. [[CrossRef](#)] [[PubMed](#)]
2. Woolf, D.N.; Kadlec, E.A.; Bethke, D.; Grine, A.D.; Nogan, J.J.; Cederberg, J.G.; Burckel, D.B.; Luk, T.S.; Shaner, E.A.; Hensley, J.M. High-efficiency thermophotovoltaic energy conversion enabled by a metamaterial selective emitter. *Optica* **2018**, *5*, 213–218. [[CrossRef](#)]
3. Sreekanth, K.V.; Alapan, Y.; Elkabbash, M.; Ilker, E.; Hinczewski, M.; Gurkan, U.A.; De Luca, A.; Strangi, G. Extreme sensitivity biosensing platform based on hyperbolic metamaterials. *Nat. Mater.* **2016**, *15*, 621–627. [[CrossRef](#)] [[PubMed](#)]
4. Liang, Y.; Li, L.; Lu, M.; Yuan, H.; Long, Z.; Peng, W.; Xu, T. Comparative investigation of sensing behaviors between gap and lattice plasmon modes in a metallic nanoring array. *Nanoscale* **2018**, *10*, 548–555. [[CrossRef](#)] [[PubMed](#)]
5. Sang, T.; Wang, R.; Li, J.; Zhou, J.; Wang, Y. Approaching total absorption of graphene strips using a c-Si subwavelength periodic membrane. *Opt. Commun.* **2018**, *413*, 255–260. [[CrossRef](#)]
6. Park, H.; Crozier, K.B. Vertically Stacked Photodetector Devices Containing Silicon Nanowires with Engineered Absorption Spectra. *ACS Photonics* **2015**, *2*, 544–549. [[CrossRef](#)]
7. Lin, H.; Sturmberg, B.C.P.; Lin, K.T.; Yang, Y.; Zheng, X.; Chong, T.K.; de Sterke, C.M.; Jia, B. A 90-nm-thick graphene metamaterial for strong and extremely broadband absorption of unpolarized light. *Nat. Photonics* **2019**, *13*, 270–276. [[CrossRef](#)]
8. Zhu, L.; Raman, A.P.; Fan, S. Radiative cooling of solar absorbers using a visibly transparent photonic crystal thermal blackbody. *Proc. Natl. Acad. Sci. USA* **2015**, *112*, 12282–12287. [[CrossRef](#)]
9. Zhou, L.; Tan, Y.; Ji, D.; Zhu, B.; Zhang, P.; Xu, J.; Gan, Q.; Yu, Z.; Zhu, J. Self-assembly of highly efficient, broadband plasmonic absorbers for solar steam generation. *Sci. Adv.* **2016**, *2*, e1501227. [[CrossRef](#)]
10. Park, H.; Dan, Y.; Seo, K.; Yu, Y.J.; Duane, P.K.; Wober, M.; Crozier, K.B. Filter-Free Image Sensor Pixels Comprising Silicon Nanowires with Selective Color Absorption. *Nano Lett.* **2014**, *14*, 1804–1809. [[CrossRef](#)]
11. Richner, P.; Eghlidi, H.; Kress, S.J.P.; Schmid, M.; Norris, D.J.; Poulidakos, D. Printable Nanoscopic Metamaterial Absorbers and Images with Diffraction-Limited Resolution. *ACS Appl. Mater. Interfaces* **2016**, *8*, 11690–11697. [[CrossRef](#)]
12. Ito, M.M.; Gibbons, A.H.; Qin, D.; Yamamoto, D.; Jiang, H.; Yamaguchi, D.; Tanaka, K.; Sivaniah, E. Structural colour using organized microfibrillation in glassy polymer films. *Nature* **2019**, *570*, 363–367. [[CrossRef](#)]
13. Landy, N.I.; Sajuyigbe, S.; Mock, J.J.; Smith, D.R.; Padilla, W.J. Perfect Metamaterial Absorber. *Phys. Rev. Lett.* **2008**, *100*, 207402. [[CrossRef](#)]

14. Lee, B.J.; Wang, L.P.; Zhang, Z.M. Coherent thermal emission by excitation of magnetic polaritons between periodic strips and a metallic film. *Opt. Express* **2008**, *16*, 11328–11336. [[CrossRef](#)]
15. Hao, J.; Zhou, L.; Qiu, M. Nearly total absorption of light and heat generation by plasmonic metamaterials. *Phys. Rev. B* **2011**, *83*, 165107. [[CrossRef](#)]
16. Fang, Z.; Zhen, Y.-R.; Fan, L.; Zhu, X.; Nordlander, P. Tunable wide-angle plasmonic perfect absorber at visible frequencies. *Phys. Rev. B* **2012**, *85*, 245401. [[CrossRef](#)]
17. Liu, N.; Mesch, M.; Weiss, T.; Hentschel, M.; Giessen, H. Infrared Perfect Absorber and Its Application as Plasmonic Sensor. *Nano Lett.* **2010**, *10*, 2342–2348. [[CrossRef](#)]
18. Aydin, K.; Ferry, V.E.; Briggs, R.M.; Atwater, H.A. Broadband polarization-independent resonant light absorption using ultrathin plasmonic super absorbers. *Nat. Commun.* **2011**, *2*, 517. [[CrossRef](#)]
19. Liu, H.; Liu, K.; Wang, L.; Jiang, S.; Zeng, W. Multimodal Broadband Plasmonic Absorber with Densely Packed Metallic Nanostars. *IEEE Photonics Technol. Lett.* **2015**, *27*, 786–789. [[CrossRef](#)]
20. Rana, A.S.; Mehmood, M.Q.; Jeong, H.; Kim, I.; Rho, J. Tungsten-based Ultrathin Absorber for Visible Regime. *Sci. Rep.* **2018**, *8*, 2443. [[CrossRef](#)]
21. Wu, J. Absorption enhancement in thin-film solar cells based on periodically chirped structure. *Sol. Energy* **2018**, *165*, 85–89. [[CrossRef](#)]
22. Sang, T.; Gao, J.; Yin, X.; Qi, H.; Wang, L.; Jiao, H. Angle-insensitive broadband absorption enhancement of graphene using a multi-grooved metasurface. *Nanoscale Res. Lett.* **2019**, *14*, 105. [[CrossRef](#)]
23. Wang, H.; Wang, L. Perfect selective metamaterial solar absorbers. *Opt. Express* **2013**, *21*, A1078–A1093. [[CrossRef](#)]
24. Guo, W.; Liu, Y.; Han, T. Ultra-broadband infrared metasurface absorber. *Opt. Express* **2016**, *24*, 20586–20592. [[CrossRef](#)]
25. Ghobadi, A.; Hajian, H.; Gokbayrak, M.; Dereshgi, S.A.; Toprak, A.; Butun, B.; Ozbay, E. Visible light nearly perfect absorber: An optimum unit cell arrangement for near absolute polarization insensitivity. *Opt. Express* **2017**, *25*, 27624–27634. [[CrossRef](#)]
26. Li, Z.; Stan, L.; Czaplowski, D.A.; Yang, X.; Gao, J. Wavelength-selective mid-infrared metamaterial absorbers with multiple tungsten cross resonators. *Opt. Express* **2018**, *26*, 5616–5631. [[CrossRef](#)]
27. Huang, Y.; Liu, L.; Pu, M.; Li, X.; Ma, X.; Luo, X. A refractory metamaterial absorber for ultra-broadband, omnidirectional and polarization-independent absorption in the UV-NIR spectrum. *Nanoscale* **2018**, *10*, 8298–8303. [[CrossRef](#)]
28. High, A.A.; Devlin, R.C.; Dibos, A.; Polking, M.; Wild, D.S.; Perczel, J.; De Leon, N.P.; Lukin, M.D.; Park, H. Visible-frequency hyperbolic metasurface. *Nature* **2015**, *522*, 192–196. [[CrossRef](#)]
29. Guo, Z.; Jiang, H.; Chen, H. Hyperbolic metamaterials: From dispersion manipulation to applications. *J. Appl. Phys.* **2020**, *127*, 071101. [[CrossRef](#)]
30. Yang, X.; Yao, J.; Rho, J.; Yin, X.; Zhang, X. Experimental realization of three-dimensional indefinite cavities at the nanoscale with anomalous scaling laws. *Nat. Photonics* **2012**, *6*, 450–454. [[CrossRef](#)]
31. Song, J.; Zhou, W. Multiresonant Composite Optical Nanoantennas by Out-of-plane Plasmonic Engineering. *Nano Lett.* **2018**, *18*, 4409–4416. [[CrossRef](#)]
32. Maccaferri, N.; Zhao, Y.; Isoniemi, T.; Iarossi, M.; Parracino, A.; Strangi, G.; De Angelis, F. Hyperbolic Meta-Antennas Enable Full Control of Scattering and Absorption of Light. *Nano Lett.* **2019**, *19*, 1851–1859. [[CrossRef](#)]
33. Isoniemi, T.; Maccaferri, N.; Ramasse, Q.M.; Strangi, G.; De Angelis, F. Electron Energy Loss Spectroscopy of Bright and Dark Modes in Hyperbolic Metamaterial Nanostructures. *Adv. Opt. Mater.* **2020**, *8*, 200277. [[CrossRef](#)]
34. Caligiuri, V.; Pezzi, L.; Veltri, A.; De Luca, A. Resonant Gain Singularities in 1D and 3D Metal/Dielectric Multilayered Nanostructures. *ACS Nano* **2016**, *11*, 1012–1025. [[CrossRef](#)]
35. Guclu, C.; Luk, T.S.; Wang, G.T.; Capolino, F. Radiative emission enhancement using nano-antennas made of hyperbolic metamaterial resonators. *Appl. Phys. Lett.* **2014**, *105*, 123101. [[CrossRef](#)]
36. Lu, D.; Kan, J.J.; Fullerton, E.E.; Liu, Z. Enhancing spontaneous emission rates of molecules using nanopatterned multilayer hyperbolic metamaterials. *Nat. Nanotechnol.* **2014**, *9*, 48–53. [[CrossRef](#)]
37. Indukuri, S.R.K.C.; Bar-David, J.; Mazurski, N.; Levy, U. Ultrasmall Mode Volume Hyperbolic Nanocavities for Enhanced Light–Matter Interaction at the Nanoscale. *ACS Nano* **2019**, *13*, 11770–11780. [[CrossRef](#)]

38. Maccaferri, N.; Isoniemi, T.; Hinczewski, M.; Iarossi, M.; Strangi, G.; De Angelis, F. Designer Bloch plasmonpolariton dispersion in grating-coupled hyperbolic metamaterials. *APL Photonics* **2020**, *5*, 076109. [[CrossRef](#)]
39. Riley, C.T.; Smalley, J.S.T.; Brodie, J.R.J.; Fainman, Y.; Sirbuly, D.J.; Liu, Z. Near-perfect broadband absorption from hyperbolic metamaterial nanoparticles. *Proc. Natl. Acad. Sci. USA* **2017**, *114*, 1264–1268. [[CrossRef](#)]
40. Abdelatif, G.Y.; Hameed, M.F.O.; Obayya, S.S.A.; Hussein, M. Ultrabroadband absorber based on a funnel-shaped anisotropic metamaterial. *J. Opt. Soc. Am. B* **2019**, *36*, 2889–2895. [[CrossRef](#)]
41. Sakhdari, M.; Hajizadegan, M.; Farhat, M.; Chen, P.-Y. Efficient, broadband and wide-angle hot-electron transduction using metal-semiconductor hyperbolic metamaterials. *Nano Energy* **2016**, *26*, 371–381. [[CrossRef](#)]
42. Cui, Y.; Fung, K.H.; Xu, J.; Ma, H.; Jin, Y.; He, S.; Fang, N.X. Ultrabroadband light absorption by a sawtooth anisotropic metamaterial slab. *Nano Lett.* **2012**, *12*, 1443–1447. [[CrossRef](#)]
43. Ji, D.; Song, H.; Zeng, X.; Hu, H.; Liu, K.; Zhang, N.; Gan, Q. Broadband absorption engineering of hyperbolic metafilm patterns. *Sci. Rep.* **2014**, *4*, 4498. [[CrossRef](#)]
44. Zhou, J.; Kaplan, A.F.; Chen, L.; Guo, L.J. Experiment and Theory of the Broadband Absorption by a Tapered Hyperbolic Metamaterial Array. *ACS Photonics* **2014**, *1*, 618–624. [[CrossRef](#)]
45. Hoa, N.T.Q.; Lam, P.H.; Tung, P.D.; Tuan, T.S.; Nguyen, H. Numerical study of a wide-angle and polarization-insensitive ultrabroadband and metamaterial absorber in visible and nearinfrared region. *IEEE Photonics J.* **2019**, *11*, 4600208. [[CrossRef](#)]
46. Hu, S.; Yang, S.; Liu, Z.; Quan, B.; Li, J.; Gu, C. Broadband and Polarization-Insensitive Absorption Based on a Set of Multisized Fabry-Perot-like Resonators. *J. Phys. Chem. C* **2019**, *123*, 13856–13862. [[CrossRef](#)]
47. Lin, Y.; Cui, Y.; Ding, F.; Fung, K.H.; Ji, T.; Li, D.; Hao, Y. Tungsten based anisotropic metamaterial as an ultra-broadband absorber. *Opt. Mater. Express* **2017**, *7*, 606–617. [[CrossRef](#)]
48. Liang, Q.; Wang, T.; Lu, Z.; Sun, Q.; Fu, Y.; Yu, W. Metamaterial-Based Two Dimensional Plasmonic Subwavelength Structures Offer the Broadest Waveband Light Harvesting. *Adv. Opt. Mater.* **2013**, *1*, 43–49. [[CrossRef](#)]
49. Ding, F.; Jin, Y.; Li, B.; Cheng, H.; Mo, L.; He, S. Ultrabroadband strong light absorption based on thin multilayered metamaterials. *Laser Photonics Rev.* **2014**, *8*, 946–953. [[CrossRef](#)]
50. Tsakmakidis, K.L.; Boardman, A.D.; Hess, O. ‘Trapped rainbow’ storage of light in metamaterials. *Nature* **2007**, *450*, 397–401. [[CrossRef](#)]
51. Hu, H.; Ji, D.; Zeng, X.; Liu, K.; Gan, Q. Rainbow Trapping in Hyperbolic Metamaterial Waveguide. *Sci. Rep.* **2013**, *3*, 1249. [[CrossRef](#)] [[PubMed](#)]
52. Rakić, A.D.; Djurišić, A.B.; Elazar, J.M.; Majewski, M.L. Optical properties of metallic films for vertical-cavity optoelectronic devices. *Appl. Opt.* **1998**, *37*, 5271–5283. [[CrossRef](#)] [[PubMed](#)]
53. FDTD Solutions. Available online: <https://www.lumerical.com/products/fdtd/> (accessed on 18 August 2020).
54. Deng, G.; Song, X.; Dereshgi, S.A.; Xu, H.; Aydin, K. Tunable multi-wavelength absorption in mid-IR region based on a hybrid patterned graphene-hBN structure. *Opt. Express* **2019**, *27*, 23576–23584. [[CrossRef](#)] [[PubMed](#)]
55. Smith, D.R.; Vier, D.C.; Koschny, T.; Soukoulis, C.M. Electromagnetic parameter retrieval from inhomogeneous metamaterials. *Phys. Rev. E* **2005**, *71*, 036617. [[CrossRef](#)] [[PubMed](#)]
56. Sang, T.; Gao, J.; Wang, L.; Qi, H.; Yin, X.; Wang, Y. Numerical study of angle-insensitive and tunable dual-band THz absorber using periodic cross-shaped graphene arrays. *Materials* **2019**, *12*, 2063. [[CrossRef](#)]
57. Artar, A.; Yanik, A.A.; Altug, H. Fabry-Pérot nanocavities in multilayered plasmonic crystals for enhanced biosensing. *Appl. Phys. Lett.* **2009**, *95*, 051105. [[CrossRef](#)]
58. Eksioğlu, Y.; Cetin, A.E.; Petracek, J. Optical response of plasmonic nanohole arrays comparison of square and hexagonal lattices. *Plasmonics* **2016**, *11*, 851–856. [[CrossRef](#)]
59. Pors, A.; Bozhevolnyi, S.I. Efficient and broadband quarter-wave plates by gap-plasmon resonators. *Opt. Express* **2013**, *21*, 2942–2952. [[CrossRef](#)]
60. Hendrickson, J.R.; Vangala, S.; Dass, C.K.; Gibson, R.; Goldsmith, J.; Leedy, K.D.; Walker, D.E.; Cleary, J.W.; Kim, W.; Guo, J. Coupling of Epsilon-Near-Zero Mode to Gap Plasmon Mode for Flat-Top Wideband Perfect Light Absorption. *ACS Photonics* **2018**, *5*, 776–781. [[CrossRef](#)]
61. Wang, X.; Sang, T.; Qi, H.; Li, G.; Yin, X.; Wang, Y. Cascaded Nanorod Arrays for Ultrabroadband, Omnidirectional and Polarization-Insensitive Absorption. *Appl. Sci.* **2020**, *10*, 3878. [[CrossRef](#)]

62. Bai, Y.; Zhao, L.; Ju, D.; Jiang, Y.; Liu, L. Wide-angle, polarization-independent and dual-band infrared perfect absorber based on L-shaped metamaterial. *Opt. Express* **2015**, *23*, 8670–8680. [[CrossRef](#)] [[PubMed](#)]
63. Cheng, Y.; Gong, R.; Cheng, Z. A photoexcited broadband switchable metamaterial absorber with polarization-insensitive and wide-angle absorption for terahertz waves. *Opt. Commun.* **2016**, *361*, 41–46. [[CrossRef](#)]



© 2020 by the authors. Licensee MDPI, Basel, Switzerland. This article is an open access article distributed under the terms and conditions of the Creative Commons Attribution (CC BY) license (<http://creativecommons.org/licenses/by/4.0/>).